

# Time-domain modelling and thermometry of the CH<sub>4</sub> $\nu_1$ Q-branch using hybrid femtosecond/picosecond coherent anti-Stokes Raman scattering

Timothy Y. Chen<sup>a</sup>, Christopher J. Kliewer<sup>b,\*</sup>, Benjamin M. Goldberg<sup>b,1</sup>, Egemen Kolemen<sup>a,c</sup>, and Yiguang Ju<sup>a</sup>

<sup>a</sup>*Department of Mechanical and Aerospace Engineering, Princeton University, Princeton, NJ 08544, USA*

<sup>b</sup>*Sandia National Laboratories, Livermore, CA 94550, USA*

<sup>c</sup>*Princeton Plasma Physics Laboratory, Princeton, NJ 08543, USA*

*\*Corresponding author: cjkliw@sandia.gov*

## Abstract

We present time-domain measurements and modelling of the CH<sub>4</sub>  $\nu_1$  vibrational Q-branch, as well as simultaneous temperature acquisition from the CH<sub>4</sub> and N<sub>2</sub> vibrational Q-branches using broadband hybrid femtosecond/picosecond coherent anti-Stokes Raman scattering (fs/ps CARS). Accurate measurements with fs/ps CARS require knowledge of the time-domain response of the probed molecule at different temperatures and pressures. In this work, a fs/ps CARS model was developed for the CH<sub>4</sub>  $\nu_1$  Q-branch and validated using time-resolved probe delay scans at pressures between 70 and 600 Torr and temperatures between 295 and 1000 K. A simplified modified exponential energy gap model was used to determine the linewidths of the Raman transitions within the Q-branch. Total Q-branch linewidths for the entire explored parameter space were also determined from the probe delay scans. This enabled quantitative measurements of CH<sub>4</sub> with fs/ps CARS as well as the temperature through the hot bands of the CH<sub>4</sub>  $\nu_1$  Q-branch. With a broadband fs laser pulse in a two-beam phase matching scheme, the N<sub>2</sub> Q-branch and CH<sub>4</sub>  $\nu_1$  Q-branch were simultaneously measured in a heated cell, and the temperatures from each molecule's spectra was evaluated. The fitted temperatures corresponded well with differences ranging from 4 to 17%. It was also shown that exchanging 90% of CH<sub>4</sub> for N<sub>2</sub> or Ar at 295 K and 500 Torr did not significantly impact the normalized time-domain signal prior to a 100 picosecond probe delay. Spatially resolved one-dimensional (1-D) thermometry using the CH<sub>4</sub> Q-branch was also demonstrated with an imaged spatial resolution of 40 microns. With the developed model, 1-D quantitative measurements of CH<sub>4</sub> concentration and temperature can be measured with time resolution of tens of picoseconds.

*Keywords:* Laser diagnostics, coherent anti-Stokes Raman scattering, thermometry, femtosecond/picosecond CARS, methane, ultrafast spectroscopy

## 1. Introduction

Methane is a major component in natural gas and there is significant interest in its usage for power generation [1], vehicle engines [2], carbon nanomaterials [3], and chemical reforming [4–7] to more valuable higher hydrocarbons. Furthermore, methane is a potent greenhouse gas, and further development of efficient chemical or energy conversion of methane into valuable carbon materials, hydrogen, and chemicals will be important for limiting global temperature increases to below 1.5°C [8]. Therefore, it is necessary to be

1. Present address: Lawrence Livermore National Laboratory, Livermore, CA 94550, United States of America

able to quantitatively detect the time history of number density and temperature of methane molecules in non-equilibrium heterogeneous reactive systems with high spatial resolution, particularly near solid-gas interfaces.

Laser-based *in-situ* detection of methane and its use as a probe molecule for thermometry and speciation is well-established, particularly with absorption [9–15] and Raman techniques [16–24]. Laser absorption spectroscopy of CH<sub>4</sub>, particularly with tunable diode lasers in the mid-infrared, have shown high sensitivity even in harsh environments, such as shock tubes for kinetic studies. For instance, detection sensitivity of CH<sub>4</sub> below 10 parts-per-million was demonstrated in a C<sub>3</sub>H<sub>8</sub> pyrolysis shock tube experiment, capturing a 1 millisecond time-series with sub-microsecond time resolution [14]. However, laser absorption is integrated across the line-of-sight, making localized measurements along the laser propagation direction difficult to achieve. In addition, pressure-broadening coefficients in mixtures other than air are not well-documented in databases like HITRAN [25], requiring separate calibration as was done in [14]. Furthermore, thermometry typically requires frequency scanning across at least two absorption features, which limits the time resolution to the scanning speed [26]. Using a chirped supercontinuum laser alleviates this issue due to the pulsed nature of the laser, but the measurement is still path integrated [15]. Spatially resolved spontaneous Raman scattering measurements simultaneously imaged along the laser propagation direction are possible and such measurements have been conducted in flames and non-equilibrium plasmas [27,28]. However, spontaneous Raman scattering is a weak process with cross-sections over three orders of magnitude smaller than those of Rayleigh scattering [29,30]. This requires the use of high energy lasers for sufficient signal, such as in [24] where four lasers were employed to achieve 1.4 J of pulse energy across 400 ns without optical breakdown. Coherently driving the Raman process can overcome limitations from the small spontaneous Raman cross-sections. One such method is coherent anti-Stokes Raman scattering (CARS), which can enhance the Raman signal by several orders of magnitude [31] when using nanosecond pulse width lasers (ns CARS). This enabled acquisition of spatially resolved one-dimensional Raman images in flames [32,33]. However, a major challenge for ns CARS is the elimination of the non-resonant background from four wave mixing and methods for non-resonant background suppression have been developed over the years [34–36]. However, these methods can reduce the signal by a factor of 2 or more.

In this work, we further develop an ultrafast variant of CARS, hybrid femtosecond/picosecond coherent anti-Stokes Raman scattering (fs/ps CARS) [37–49], for detection and thermometry of the CH<sub>4</sub>  $\nu_1$  symmetric stretch vibrational Raman Q-branch. The advantages of fs/ps CARS include simultaneous detection of many Raman transitions using a broadband femtosecond laser with tens to hundreds of microns of spatial resolution [41,49]. The non-resonant background is avoided by delaying the spectrally narrow picosecond probe pulse with respect to the femtosecond pulse such that they do not overlap in time. With high intensity ultrashort pulses, the nonlinear optical interaction is significantly enhanced compared to ns CARS. The high peak intensity enables highly localized near surface measurements with one dimensional spatial resolution normal to the surface [49–51] or two dimensional images [42] with picosecond temporal resolution. In addition, methane as a probe molecule is attractive due to its high polarizability and correspondingly large Raman cross-section for the  $\nu_1$  Q-branch, which is 8.6 times that of the N<sub>2</sub> Q-branch [52]. For CARS, the signal intensity scales with the square of the Raman

cross-section, making CH<sub>4</sub> signals more than 70 times stronger than N<sub>2</sub> Q-branch signals. Moreover, in applications like methane reforming, only methane is the major species and no nitrogen exists.

In the past four decades, the CH<sub>4</sub>  $\nu_1$  symmetric stretch Q-branch spectrum has been successfully characterized with high spectral resolution using stimulated Raman scattering (SRS) [53], ns CARS [19–21], and continuous wave CARS (CW CARS) [16–18]. For instance in [17], the rotational structure of the  $\nu_1$  Q-branch was resolved and assigned with 0.002 cm<sup>-1</sup> using CW CARS. However, an in-depth characterization of the CH<sub>4</sub>  $\nu_1$  hot band and validated set of Raman transition frequencies and intensities has only been recently available for simulating CARS and spontaneous Raman scattering hot CH<sub>4</sub>  $\nu_1$  Q-branch spectra [21–24]. In these works, CARS and spontaneous Raman scattering measurements of CH<sub>4</sub> at different temperatures were used to verify the capability of the CH<sub>4</sub>  $\nu_1$  Q-branch for thermometry. However, to our knowledge, a similar effort for using fs/ps CARS to perform CH<sub>4</sub> thermometry has not been reported.

In fs/ps CARS, the frequency difference of the pump and Stokes photons provided by the femtosecond laser coherently couples with the ro-vibrational energy levels of the probed molecules. The time delayed picosecond probe scatters off the established coherence and produces the anti-Stokes Raman signal photons. Since the probe laser is delayed, the coherently excited ro-vibrational modes decay depending on the lifetime of the Raman transitions and their decay rates. For an isolated Raman transition, the exponential decay time constant,  $\tau$ , can be related to the Raman Lorentzian linewidth,  $\Gamma$ , via the relationship:  $\Gamma = (2\pi c\tau)^{-1}$ , where  $c$  is the speed of light. This can be understood on the basis that the Fourier transform of a decaying complex exponential function is the Lorentzian function [54]. On the picosecond time scale of the probe delays, the linewidths are assumed to be governed by collisional rotational energy transfer [39]. As a result, accurate models of the decay rates including collisional energy transfer in the time-domain or the Raman line widths in the frequency-domain are necessary when interpreting fs/ps CARS spectra. Furthermore, if the pressure dependences of the linewidths are known, they can be exploited to make simultaneous pressure, concentration, and temperature measurements [55,56]. A significant portion of the literature focuses on directly measuring these linewidths in the time domain using time-resolved CARS [40,57–60]. However, only diatomic molecules like N<sub>2</sub> and O<sub>2</sub> and some simple triatomic molecules like CO<sub>2</sub> have been measured in detail.

Frequency-resolved point and 1-D fs/ps CARS measurements of CH<sub>4</sub> have been conducted in previous studies [43,47,50], but so far only [47] has performed fs/ps CARS time-domain measurements. In this work, the CH<sub>4</sub>  $\nu_1$  Q-branch was treated as a single Raman transition and the linewidth was determined for varying mole fractions of CH<sub>4</sub> diluted in N<sub>2</sub> at atmospheric pressure and ambient temperature. The measured linewidth was found to be insensitive to the gas mixture composition. However, the time delay scan was only measured up to 100 ps. Time-domain ps CARS measurements were reported in a supersonic CH<sub>4</sub> jet at rotational temperatures from 25 K to 80 K and a pressure of 5 atm [61,62]. The Fourier-transform of the simulated frequency-domain spectrum showed good agreement with the time-domain scan. However, measurements at higher temperatures, conditions where more rotational lines would be active, have not been conducted.

For ns-CARS measurements of the CH<sub>4</sub>  $\nu_1$  Q-branch, the linewidths have been determined through quantum models [63] and semi-classical calculations [20,21]. Semi-

classical calculations require knowledge of the interaction potential between the binary collision partners and rely on empirical infrared absorption data from the infrared-active  $\nu_3$  Q-branch for unavailable  $\nu_1$  Q-branch parameters. It would be preferable to construct a simplified linewidth model using a scaling law directly validated by time-domain data obtained from the  $\nu_1$  Raman Q-branch across different pressures and temperatures. For the  $N_2$  vibrational Q-branch, the modified exponential gap (MEG) scaling law has been successfully used for fitting the rotational energy transfer rate matrix from 0-1 atm and 295 K to 2200 K [39]. The MEG scaling parameters were also fitted for pure rotational S-branch linewidths of  $N_2$  and  $O_2$  [57,64,65]. In tetrahedral molecules such as  $SiH_4$  [66] and deuterated methane isotopes,  $CHD_3$  [67] and  $CD_4$  [68], state-to-state rotational energy transfer rates were measured by infrared double resonance spectroscopy and successfully fitted using exponential energy gap scaling laws. Therefore, it appears justified to use an exponential energy gap scaling law as the basis for fitting the linewidths of the ro-vibrational transitions of the  $CH_4 \nu_1$  Q-branch.

In this study, we use the MEG scaling law to approximate the linewidths of the rotational transitions within the  $\nu_1$  Q-branch. We use the Raman transition frequencies and intensities from [23] calculated by the Spherical top data system (STDS) software [69] and fit measured probe time delay series scanned up to 1.6 ns. These delay scans were performed at room temperature and pressures ranging from 70 Torr to 500 Torr. This constrains the pressure dependent terms of the exponential energy gap law. The temperature dependent terms were determined from high temperature spectra and delay scans in a tube furnace set to temperatures up to 1000K and pressures from 70 Torr to 600 Torr. The fitted temperatures determined by  $CH_4$  were compared against temperatures determined by simultaneously acquired  $N_2$  Q-branch spectra in  $CH_4/N_2$  mixtures at temperatures up to 1000 K. Spatially resolved 1-D fs/ps CARS thermometry was also demonstrated using spectral fits of the  $CH_4 \nu_1$  Q-branch. With this set of data, we validate the  $CH_4$  fs/ps CARS model and extend the capabilities of fs/ps CARS to quantitative 1-D  $CH_4$  sensing and thermometry.

## 2. Computational and experimental methods

### 2.1 $CH_4$ fs/ps CARS modelling approach

The principles underlying fs/ps CARS modelling in the time and frequency domains was developed previously [39,49]. Only a brief treatment as well as considerations for modelling  $CH_4$  spectra will be given here. In general, CARS is a third-order optical nonlinearity, where the pump and Stokes photons match a resonant ro-vibrational energy level of a molecule. The probe photons scatter off this resonance and the anti-Stokes Raman photons coherently propagate in the direction determined by the phase-matching conditions of the experiment. The anti-Stokes photons are then detected as the CARS signal. For fs/ps CARS, the probe is time-delayed with respect to the pump and Stokes photons. The intensity of the fs/ps CARS signal can be expressed as a function of time, assuming instantaneous electronic dephasing [39]:

$$I_{CARS}(t) \propto |P^{(3)}(t)|^2 = \left| \left( \frac{i}{\hbar} \right)^3 E_{probe}(t) \int_0^\infty dt_2 \left( R_{CARS}(t_2) \times E_{Stokes}^*(t + \tau_{23} - t_2) \times E_{pump}(t + \tau_{23} + \tau_{12} - t_2) \right) \right|^2 \quad (1)$$

where  $P^3(t)$  is the third-order polarization,  $E_{probe}$  and  $E_{pump}$  are the probe and pump electric fields,  $E_{Stokes}^*$  is the complex conjugate of the Stokes electric field,  $\tau_{12}$  is the time delay between the pump and Stokes beams,  $\tau_{23}$  is the time delay between the Stokes and probe beams, and  $t_2$  is an integration variable representing the coherence time scale between the pump/Stokes and the probe beams. The CARS molecular response,  $R_{CARS}$ , can be written as:

$$R_{CARS}(t) = \sum_v \sum_J I_{v,J_i \rightarrow v+1,J_f} \exp\left(\frac{t}{\hbar} \left( i\Delta E_{v,J_i \rightarrow v+1,J_f} - \frac{1}{2}\Gamma_{v,J_i \rightarrow v+1,J_f} \right)\right) \quad (2)$$

where  $I_{v,J_i \rightarrow v+1,J_f}$  is the Boltzmann-weighted Raman transition intensity,  $\Delta E_{v,J_i \rightarrow v+1,J_f}$  is the energy level difference of the vibrational Raman Q-branch transition,  $\Gamma_{v,J_i \rightarrow v+1,J_f}$  is the Raman linewidth,  $v$  is the vibrational quantum number,  $J_i$  is the initial rotational quantum number, and  $J_f$  is the final rotational quantum number. The Raman transition intensities were pre-calculated for different temperatures according to the partition function scaling method from [23]. Note that while  $v + 1$  is written as the final vibrational state, CH<sub>4</sub> has four vibrational modes. The notation refers to the vibrational quantum number increase of the  $\nu_1$  symmetric stretch vibrational mode, which produces the  $\nu_1$  vibrational Q-branch spectra.

The Raman linewidths are calculated using the modified exponential gap law [70,71]:

$$\Gamma_{ji} = p\alpha \left(\frac{T}{T_0}\right)^{-n} \left(\frac{1+a\hbar\omega_{v+1,J_i}/k_B T \delta}{1+a\hbar\omega_{v+1,J_i}/k_B T}\right)^2 \times \exp(-\beta\hbar(\omega_{v+1,J_j} - \omega_{v+1,J_i})/k_B T) \quad (3)$$

$$\Gamma_{ij} = \Gamma_{ji} \frac{2J_i+1}{2J_j+1} \exp\left(\hbar(\omega_{v+1,J_j} - \omega_{v+1,J_i})/k_B T\right) \quad (4)$$

$$\Gamma_j = \sum_{i \neq j} \Gamma_{ij} \quad (5)$$

where  $\Gamma_{ji}$  is the upward collisional transition from the  $i$ th rotational state  $J_i$  to the  $j$ th rotational state  $J_j$ ,  $\Gamma_{ij}$  is the downward collisional transition of the rotational states from  $J_j$  to  $J_i$ ,  $\Gamma_j$  is the linewidth of a transition out of rotational energy level  $J_j$ ,  $p$  is the pressure in Torr,  $T$  is the temperature,  $T_0$  is the reference temperature set to 295 K,  $a$  is a species-specific constant set to 2,  $\alpha$ ,  $\beta$ ,  $\delta$ , and  $n$  are adjustable parameters in the least-squares fitting,  $\omega_{v+1,J_i}$  and  $\omega_{v+1,J_j}$  are the frequency terms representing the rotational energy gap. The rotational energy gap is calculated using the following expression for rotational energy [17,72]:

$$E_j = BJ(J+1) - DJ^2(J+1)^2 \quad (6)$$

where  $B$  and  $D$  are the rotational and centrifugal constants of CH<sub>4</sub> taken from [72] and  $J$  is the rotational quantum number.  $\omega_{v+1,J_i}$  is calculated using the harmonic oscillator approximation where it is assumed that the ro-vibrational energy is the sum of separable rotational and vibrational components. The vibrational energy is calculated from the lower state vibrational quantum numbers multiplied by the  $J=0$  vibrational frequencies, used in

[23] and taken from [73]. Several additional approximations are made in constructing this linewidth model. The linewidths for the same J but different nuclear spin (A, E, or F), are assumed to be the same. Double infrared resonance measurements [74,75] suggest that the rotational relaxation rates of CH<sub>4</sub> are similar for different nuclear spins, which to first order justifies our assumption. However, they are not identical, so this effect can be explored in the future. In addition, the line width parameters for the hot bands are not determined separately from those of the ground state. The only differences are in the initial energy levels used when calculating Eq. (3).

In this study, we use fitting in the time-domain to determine the linewidth parameters from the MEG model. For every experimental probe delay, the intensity of the CH<sub>4</sub>  $\nu_1$  Q-branch is summed and compared to a simulated library of time delay traces. This is a similar approach to [76]. From Eq. (3), there are four adjustable parameters:  $\alpha$ ,  $\beta$ ,  $\delta$  and  $n$ . The first two are optimized using room temperature spectra, with  $\delta = 1$  and  $n = 0$ . The latter two are optimized with high temperature spectra. This allows us to only vary two parameters at a time for calculation of the fitting library and reduce the number of simulated spectra by at least an order of magnitude. However, with this approach, the high temperature line widths will have a different functional form from the room temperature line widths and the two models may not converge. Therefore, the trade-off for only needing to vary two parameters at a time is that there will be two fitted linewidth models: one validated at 295 K and another validated from 500-1000 K. Efforts to determine a unified MEG expression using an expanded parameter spectral library are underway. In addition, the term  $p\alpha$  is lumped together in the simulations and later separated by dividing by the pressure. This again reduces the number of variables needed to create the fitting library.

On the top of Fig. 1, a 295 K and a 1000 K CH<sub>4</sub> CARS spectrum are plotted. The bottom sub-plots of Fig. 1 show the intensities of the individual Raman transitions that were used to calculate the full fs/ps CARS profile in the top sub-plots. At 295 K, only a single peak can be seen, since nearly all of the molecules are in the vibrational ground state. At high temperatures, hot bands arise due to CH<sub>4</sub> molecules thermally populated in the  $\nu_2$ ,  $\nu_4$ ,  $2\nu_2$ ,  $2\nu_4$ , and  $\nu_2 + \nu_4$  vibrational states. These hot bands can be seen to the left of the ground state peak. The hot bands provide temperature sensitivity to the CH<sub>4</sub> Q-branch and enable thermometry.

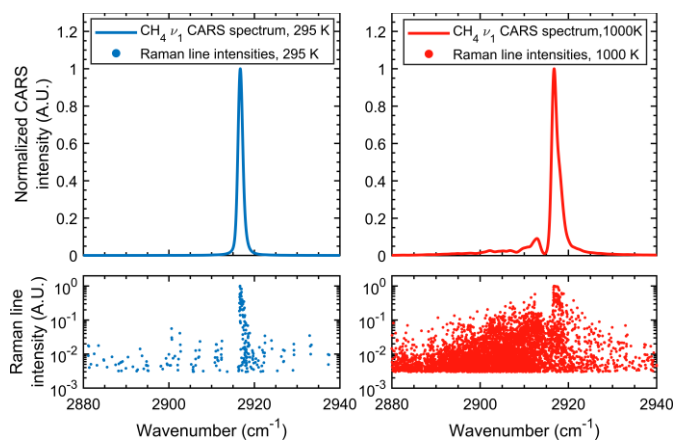


Figure 1. Simulated fs/ps CARS spectrum and Raman line intensities of CH<sub>4</sub> at 295 K (left) and 1000 K (right).

The major challenge in using the original Raman line list from [23] was the overwhelming number of transitions, over 1.7 million in total. Such a large number of transitions is not feasible for calculation and fitting of fs/ps CARS spectra in the time-domain, even with a computing cluster. To understand why, one can examine the most time-consuming step of the calculation, the molecular response function in Eq. (2). In the exponential term, the transition energy differences and linewidths must be multiplied by time. If we consider a time vector encompassing 1 ns with 1 fs time steps, that is a length of 1 million elements. Therefore, the corresponding outer product of the time vector and 1.7 million Raman transitions would result in a 1.7 million by 1 million matrix and easily exceed the memory limits of available computational resources. Therefore, a filter was used to only include transitions that were at least 0.3% as intense as the strongest transition, as seen in Fig. 1. This limited the number of considered lines to 336 at 295 K and 5901 at 1000 K. The cut off was chosen to only include transitions from the vibrational ground state at 295 K. At 1000 K, the difference in normalized spectra between a 0.001% cut off and a 0.3% cut off was below 1% in the hot band. To further increase the speed of the computations, all spectra were calculated on the graphics processing unit (GPU) nodes of the Adroit high-performance computing cluster at Princeton University. Large matrix operations, specifically in the calculation of Eq. (2), benefitted from GPU computing. A single time delay series required approximately 1 to 4 minutes on a single GPU node on the computing cluster, depending on the number of considered Raman transitions. The room temperature library contained 11,500 time delay series, and the high temperature library contained 13,000 time delay series.”

## 2.2 fs/ps CARS experimental setup and methods

The experimental setup was previously described in detail in [51] with minor changes to the focusing optics shown in Fig. 2. A brief description will be given here. The fs/ps CARS setup used a 20 Hz picosecond regenerative amplifier with a 65 ps pulse width and 6 mJ pulse energy whose oscillator was mode-locked to the oscillator of the 1 kHz fs Ti:Sapphire regenerative amplifier (Legend Elite, Coherent). The delays between the ps and fs laser pulses were controlled electronically (PDL-100A, Colby Instruments), and the maximum delay was limited by the CARS signal-to-noise ratio rather than the equipment itself. A 1.5 mJ portion of the 50 fs pulses of the Ti:Sapphire regenerative amplifier was focused into a 1 meter long hollow-core fiber filled with 400 Torr of Ar (Femtolasers). The fs pulse was spectrally broadened by self-phase modulation and compressed by negatively chirped mirrors to  $\sim 7$  fs. The bandwidth of the resultant 0.6 mJ beam was sufficient to measure both the N<sub>2</sub> Q-branch at 2330 cm<sup>-1</sup> and the CH<sub>4</sub> Q-branch at 2916 cm<sup>-1</sup> simultaneously. The fs and ps beams were cylindrically focused to the probe region with an intersection angle of 5° in a two-beam phase matching configuration. The CARS signal propagated in the phase matching direction nearly collinear with the probe beam and was separated using a short pass filter (SP01-561RU-25, Semrock). The CARS signal was imaged in a 1:1 configuration onto the 50  $\mu\text{m}$  slit of the spectrometer (iHR 550, Horiba). A 2400 gr/mm grating dispersed the signal and the CARS spectra was detected using a water-cooled charge-coupled device (CCD) with 13.5  $\mu\text{m}$  pixels (Newton 940, Andor). Dark current was minimized by cooling the CCD to -80°C and the exposure time for each spectrum was 2 seconds, accumulating for 40 laser shots per image. When necessary at high pressures, a neutral density filter was placed in front of the slit to increase the dynamic

range of the measurement. The neutral-density filter was calibrated by measuring a time delayed spectrum with and without the filter. This gave an intensity calibration factor to apply to subsequent time delays. All data was acquired in 1-D and summed across a 1 mm sheet length during post-processing. Prior to fitting, all spectra were background subtracted and divided by the non-resonant excitation profile measured in 500 Torr of Ar. For room temperature experiments, the plasma cell from [51] was used with the electrodes removed. For the high temperature experiments, an 860 mm long quartz tube with a 57 mm inner diameter was placed in a tube furnace (Carbolite) and sealed with O-rings in custom window mounts equipped with gas inlets. The windows were made from N-BK7 and were cooled by flowing compressed air on the window mounts to keep the temperature of the mounts below the melting point of the O-rings. Gas flows were regulated by mass flow controllers (MKS) and they were set to 500 SCCM. Using flowing gases ensured that pyrolysis products did not build up and contaminate the CH<sub>4</sub> Q-branch spectrum during the high temperature measurements. A downstream needle valve was used to set the pressure. At the highest set point temperature and highest pressure, 1000 K and 600 Torr, approximately 0.001% of the CH<sub>4</sub> will thermally decompose within the reactor residence time of the gas [77]. For the fs/ps CARS measurements, this was negligible and the presence of interfering hydrocarbons in the  $\nu_1$  Q-branch region was not detected

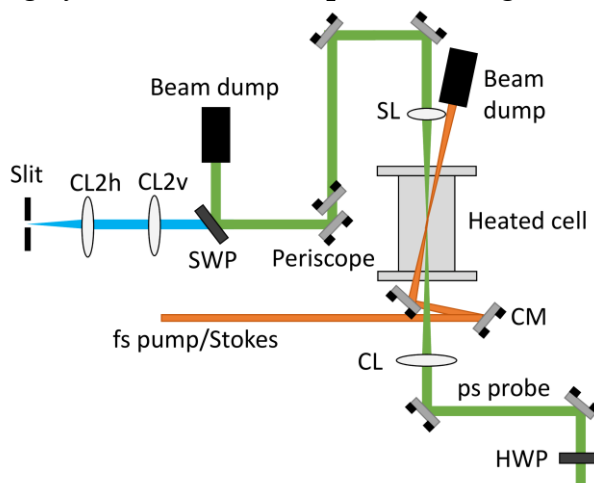


Figure 2. Experimental schematic of the fs/ps CARS setup. CM: concave cylindrical mirror with  $f = 400$  mm. CL: plano-convex cylindrical lens with  $f = 400$  mm, 400 mm, SL: spherical plano-convex lens with  $f = 400$  mm. SWP: angle-tuned short wave pass filter. HWP: half-wave plate.

### 3. Results and Discussion

#### 3.1 Room temperature measurements and modelling

The time delay traces measured for pure CH<sub>4</sub> mixtures at 295 K for pressures ranging from 70 to 500 Torr are shown in Fig. 3 as well as the fitted simulations. The parameters  $\beta$  and  $p\alpha$  were varied in a least-squares fitting routine.  $\beta$  was determined by the best fit for 300 Torr and fixed for the other pressures. Excellent agreement was obtained for time delays up to 500 ps for the pressures below 500 Torr. The coherent beat patterns matched for most of the cases, indicating that the reduced set of included Raman frequencies was adequate. However, there was some discrepancy in the fitted curve for 500 Torr from 100 ps to 200 ps. This may be due to the simplified MEG model that was

employed to fit the room temperature line widths. Either using more sophisticated linewidth calculations like semi-classical linewidth calculations or adding a third fitting variable,  $\delta$ , in the fitting routine could improve agreement. Artificially increasing  $p\alpha$  resulted in a time-domain trace that only captures the initial exponential decay and underpredicted the measurements at time delays beyond 150 ps. Overall, the fits agree well, indicating that the time-domain traces could be adequately described without considering the influence of nuclear spin symmetry. Theoretical modelling for high pressure  $\text{CH}_4$   $\nu_1$  Q-branch CARS linewidths also found that this assumption was sufficient to describe the linewidths [63].

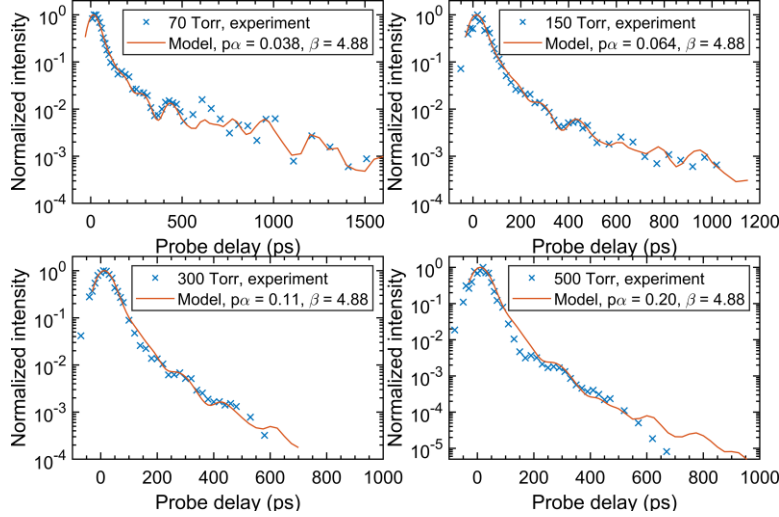


Figure 3. Experimental 295 K probe delay scans fitted with MEG parameters from pressures of 70 to 500 Torr.

Interestingly, after dividing the fitted  $p\alpha$  terms by the pressure,  $p$ , in Torr, the resulting  $\alpha$  was not constant. For the 150, 300, and 500 Torr fits, the fitted  $\alpha$  was within 10% of  $4 \times 10^{-4} \text{ cm}^{-1}/\text{Torr}$ , which was the median fitted  $\alpha$  for these three pressures. However, at 70 Torr, the fitted  $\alpha$  was  $5.4 \times 10^{-4} \text{ cm}^{-1}/\text{Torr}$ , which was 35% larger than the median  $\alpha$  for the other pressures. This indicated that  $\alpha$  was a function of pressure. This may be because each time delay trace was fitted separately with respect to  $p\alpha$  which did not guarantee the same fitted  $\alpha$  for a given pressure. However, using an  $\alpha$  of  $4 \times 10^{-4} \text{ cm}^{-1}/\text{Torr}$  for the 70 Torr time delay scan showed worse agreement at long probe delays (see Supplementary Figure S1). As a result, we used the following expression for  $\alpha$ , in  $\text{cm}^{-1}/\text{Torr}$ , determined by a linear fit to a  $p\alpha$  vs  $p$  plot (see Supplementary Figure S2) and dividing by the pressure:

$$\alpha = 5.41 \times 10^{-3} p^{-1} + 3.85 \times 10^{-4} \quad (7)$$

Equation (7) implies that at the zero-pressure limit, the product  $p\alpha$  does not become zero and therefore the linewidths do not become zero. Similar behavior was observed previously in [20,63] with the total Q-branch linewidth at room temperature having a near linear dependence on pressure with a non-zero offset if extrapolated to zero pressure. This

is a significant difference from MEG linewidth models of diatomic molecules such as N<sub>2</sub> and O<sub>2</sub> which assume constant  $\alpha$ .

As further confirmation of this phenomenon, as well as to provide useful data for future CH<sub>4</sub> CARS modelling efforts, the first 150-200 ps of the time delays were fitted with a single exponential function. The time duration that was fitted was chosen to avoid the first onset of coherent beating from closely spaced probed Raman transitions. The exponential time decay constants were extracted from the fits and then converted to linewidths using the expression  $\Gamma_{v1} = 1/(2\pi c\tau_{CARS})$ , where  $\tau_{CARS}$  is the decay constant. These linewidths are plotted in Fig. 4 along with a linear fit and the CH<sub>4</sub> Q-branch linewidth determined in [47]. The extrapolated linear fit and the literature value are within 10% and their respective uncertainty. The relatively large uncertainty in this study was due to the sparse time steps as compared to [47], since the focus here was on studying long probe delays rather than the first 100 ps. From Fig. 4, the linear fit to the total Q-branch linewidths had an  $R^2 > 0.99$  and predicted a non-zero linewidth at zero pressure. This is consistent with a pressure-dependent  $\alpha$  in the MEG model. However, additional measurements at pressures lower than 70 Torr are required to completely verify this.

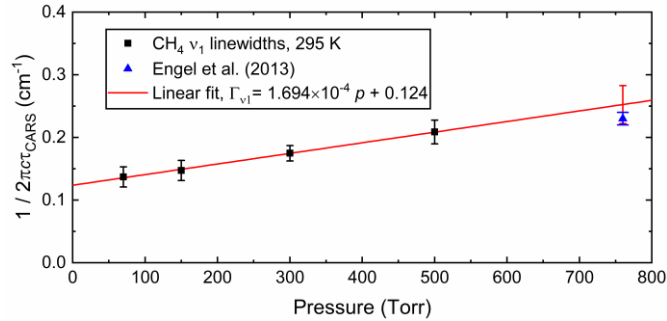


Figure 4. Fitted total Q-branch linewidths from single exponential decays of probe delay scans as a function of pressure. The atmospheric pressure linewidth from [47] was plotted along with an extrapolated linear fit.

The effect of the gas mixture was also investigated by substituting 90% of CH<sub>4</sub> with either N<sub>2</sub> or Ar at 500 Torr. The time delay traces for these three mixtures are plotted in Fig. 5. The exponential decays from Fig. 5 were fitted in the same manner as that in Fig. 4. A simulated convolution of the fs pump/Stokes pulse with the 65 ps probe pulse was plotted as the dashed time profile. The corresponding total Q-branch linewidths are reported along with the linewidths from Fig. 4 in Table 1. From Table 1, the measured linewidths of the N<sub>2</sub> and Ar mixtures do not vary significantly. Additionally, from Fig. 5, the influence of the mixture composition is only discernable after a critical probe delay, approximately 100 ps. At this probe delay, the probe pulse convolution decayed by three orders of magnitude, indicating that the overlap of the time delay curves at 100 ps was not dominated by the probe pulse width. This agreed with [47], where the mole fraction of CH<sub>4</sub> was varied from 0.1 to 1 in a N<sub>2</sub> bath gas and the atmospheric pressure CH<sub>4</sub> total Q-branch linewidth was approximately constant as measured across 100 ps probe delay scans. To explain this, we need to estimate a time scale that describes the critical probe delay for collisional partner independence. From gas kinetic theory, the probability of a molecule not experiencing a collision after time  $t$  is  $\exp(-t/\tau)$  where  $\tau$  is the mean time between collisions. For instance, at a probe delay of 40 ps in a CH<sub>4</sub> gas at 500 Torr, this probability

is 25% with a mean time between collisions of 140 ps. From the quadratic scaling of CARS with number density, such a delay ensures that 90% of the original CARS signal survives collision-free. However, this time scale is shorter than when the time-domain measurements start to diverge in Fig. 5. On the other hand, the mean time between collisions estimates a time scale longer than the measured critical probe delay. If the probability of collisions is increased to 50%, the estimated time scale would be 97 ps. This corresponds well with the measured critical probe delay in Fig. 5. Since the measurement at this probe delay is not “collision-free,” we define this time scale as the “collision sensitivity time”. This is an indication that the influence of collisional partners on the CARS dephasing is weak, and the measurement does not need to be strictly “collision-free” for collisional partner independence in the initial dephasing rates. This corresponds well with the measured critical probe delay marked in Fig. 5. For the measurements in [47], this time would correspond to around 60 ps. Therefore, most of their measured probe delays would not be expected to vary significantly with mixture composition. Whether this simple estimation works for CH<sub>4</sub> mixtures with different gases like O<sub>2</sub> and CO<sub>2</sub> and different pressures is unknown and would be worth further investigation. As stated in [47], insensitivity toward gas mixture composition would be beneficial for future quantitative measurements of CH<sub>4</sub> mole fraction. Specifically, this would be an advantage for measurements in dynamic environments such as ignition events or pulsed non-equilibrium plasmas, where the collisional environment changes with time.

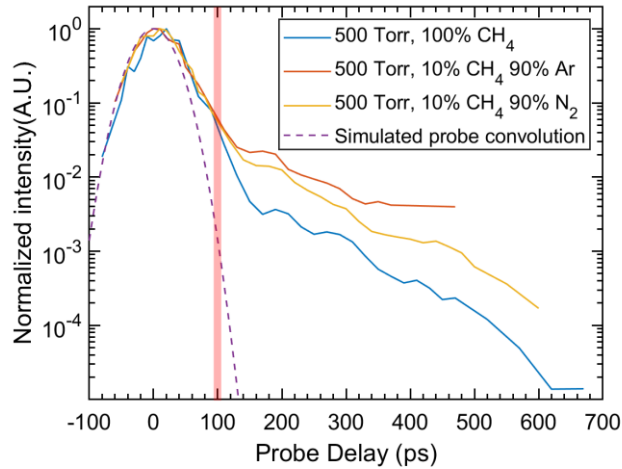


Figure 5. Probe delay scan of 500 Torr CH<sub>4</sub> mixtures. The measured critical probe delay for collisional partner independence is shaded in red.

Table 1. Total 295 K CH<sub>4</sub>  $\nu_1$  Q-branch linewidth from single exponential fits

Mixture	Pressure (Torr)	$\Gamma_{\nu_1}$ (cm <sup>-1</sup> )
Pure CH <sub>4</sub>	70	0.137 ± .016
	150	0.147 ± .016
	300	0.175 ± .012
	500	0.21 ± .02
10% CH <sub>4</sub> /90%Ar	500	0.158 ± .02

10%CH <sub>4</sub> /90%N <sub>2</sub>	500	0.167 ± .02
---------------------------------------	-----	-------------

### 3.2 High temperature measurements and modelling

After determining the best fit  $\beta$  and  $\alpha$ , these parameters were kept constant while  $\delta$  and  $n$  were varied in Eq. (3) for the high temperature linewidth model. Keeping  $\delta = 1$  like in the room temperature linewidth model and varying only  $n$  could not fit the experimental data. The experimental time delay traces as well as the simulated ones are plotted in Fig. 6. In Fig. 6, the pressure was kept constant but the temperature setpoint of the furnace was changed from 500 K to 1000 K. Only the ground state Q-branch intensity was summed for the time-domain fitting. The least squares-fitting routine simultaneously fit all of the time delay traces by defining the error function as the sum of the residuals from all three conditions. From Fig. 6, a good fit was achieved for all three temperatures up to 200 ps and again, the coherence beating was well-matched across longer time scales. To confirm that the previously determined pressure dependence still held, time delay traces measured at a fixed setpoint temperature of 1000 K and pressures from 150 Torr and 600 Torr are compared with the simulations in Fig. 7. The simulated time delay series matched well for delays up to 200 ps and qualitative agreement was achieved with the coherence beat pattern. Note, these two conditions were not used in the fit. Therefore, the 150 and 600 Torr measurements served as validation of the high temperature time-domain model. As in the room temperature time-domain measurements, the single exponential time decays were converted to linewidths and tabulated in Table 2. From Table 2, the hot band linewidths were not found to be pressure sensitive. This may indicate that collisions do not dominate the decay of the hot band region at high temperatures.

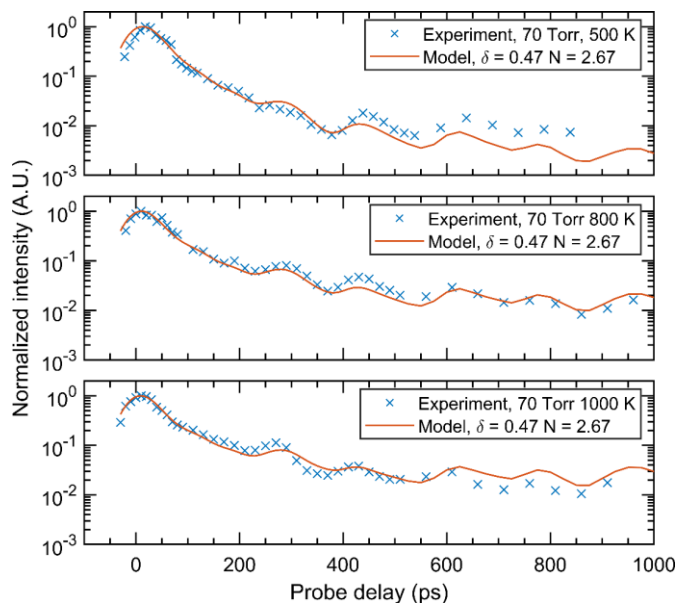


Figure 6. Experimental and fitted probe delay scans of heated CH<sub>4</sub> at 70 Torr with temperatures varying from 500 to 1000 K along.

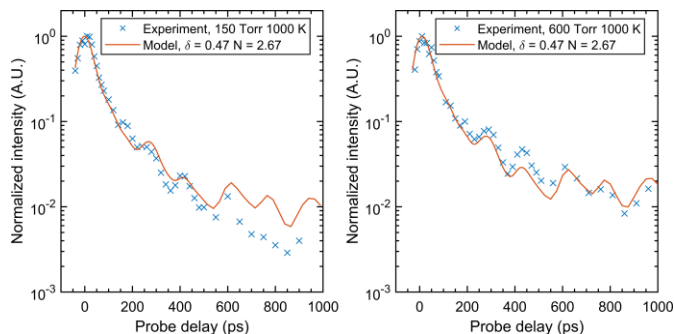


Figure 7. Probe delay scans of heated CH<sub>4</sub> at a 1000 K for pressures of 150 Torr (left) and 600 Torr (right) along with predicted time-domain curves from the MEG fits.

Table 2. Single exponential fits of the CH<sub>4</sub>  $\nu_1$  Q-branch at high temperatures.

Pressure (Torr)	Setpoint temperature (K)	$\Gamma_{\nu_1}$ (cm <sup>-1</sup> )	$\Gamma_{hot\ band}$ (cm <sup>-1</sup> )
70	295	0.137 ± .016	-
70	500	0.11 ± .014	-
70	800	0.088 ± .012	0.19 ± .05
70	1000	0.08 ± .015	0.18 ± .03
150	1000	.10 ± .01	0.17 ± .03
600	1000*	0.136 ± .02	0.18 ± .03

\*While the setpoint temperature was 1000 K, the actual temperature at the measurement location was likely lower by 14% due to increased heat losses at high pressure. See text for details.

With the linewidth parameters determined for the high temperature model, frequency-domain thermometry could be performed at various time delays. With the large bandwidth available from the hollow-core fiber, CH<sub>4</sub>  $\nu_1$  Q-branch and N<sub>2</sub> Q-branch spectra were simultaneously acquired and fitted for evaluation of temperature. An example fit of both spectra are plotted in Fig. 8. At 500 Torr and 1000 K set point, the evaluated temperature was 860 K for the CH<sub>4</sub> fit and 850 K for the N<sub>2</sub> Q-branch. The instrument function of the spectrometer was determined by fitting a Gaussian line shape to the ro-vibrational Raman transitions of the N<sub>2</sub> Q-branch spectrum measured at 500 Torr and a 1000 K setpoint. Once determined, this Gaussian line shape was applied to the CH<sub>4</sub> Q-branch spectrum for each Raman transition considered. Further comparisons between the evaluated temperatures are plotted in Fig. 9 for temperature set points of 500 K, 800 K, and 1000 K. Each data point for the CH<sub>4</sub> Q-branch was measured at either 0 ps or 50 ps delay, while the N<sub>2</sub> Q-branch temperature was the average of the spectra evaluated at 50 ps and 100 ps delays. The delays for the N<sub>2</sub> temperature evaluations were chosen to avoid non-resonant background effects. For CH<sub>4</sub>, a strong non-resonant background was not observed even at a delay of 0 ps, possibly due to its relatively large resonant Raman cross-section. At the highest measured CH<sub>4</sub> number density condition, 500 Torr and 295 K, the ratio between the resonant and non-resonant signals was at most 0.025% (see Supplementary Figure S3). Additionally, at such a large Raman shift and weak non-resonant background amplitude, the background would be nearly flat in the frequency domain and would not significantly impact the thermometry results. However, if the non-resonant background were strong, then coherent interferences due to phase offsets from the resonant signal

would become apparent in the frequency domain. Fig. 9 shows that the CH<sub>4</sub> Q-branch evaluated temperatures were consistent with those obtained from the N<sub>2</sub> Q-branch. For the lowest and highest setpoints, the discrepancy was within 4%. At the N<sub>2</sub> temperature of 730 K, the discrepancy was 8 and 17 %. This may be due to the hot band linewidths being inadequately modelled at this temperature, since the hot band linewidths were not separately fitted. A more detailed linewidth model with separate MEG parameters for the ground state Q-branch and the hot band could result in a more accurate temperature measurement.

A similar comparison with N<sub>2</sub> Q-branch measurements was previously shown with ns-CARS [21]. Differences between the two spectral regions was below 4% for temperatures under 1200 K, while a significant discrepancy was found in temperatures above 1200 K when using a flame. From [21], one suggested explanation was that the measured locations were not the exact same within their flame, since N<sub>2</sub> and CH<sub>4</sub> were measured separately. With the supercontinuum 7 fs pulse used in this study, simultaneous thermometry from both the CH<sub>4</sub> and N<sub>2</sub> Q-branches would resolve that difficulty. In addition, simultaneous thermometry can be used for studying molecular energy transfer with N<sub>2</sub> and CH<sub>4</sub>, such as in studies of hypersonic atmospheric entry of Saturn’s largest moon, Titan [78].

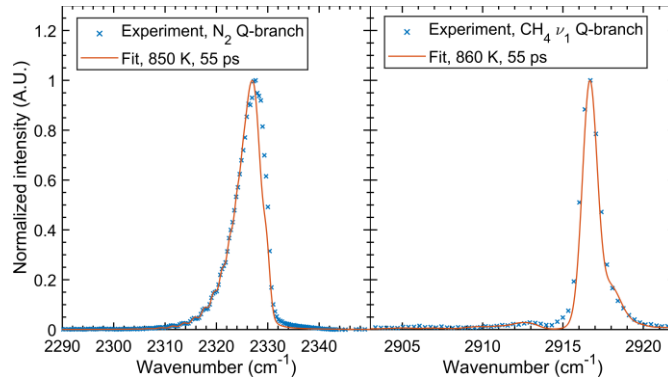


Figure 8. Simultaneously acquired CH<sub>4</sub> and N<sub>2</sub> Q-branch spectra at 500 Torr and 1000 K setpoint in a 10% CH<sub>4</sub> and 90% N<sub>2</sub> mixture.

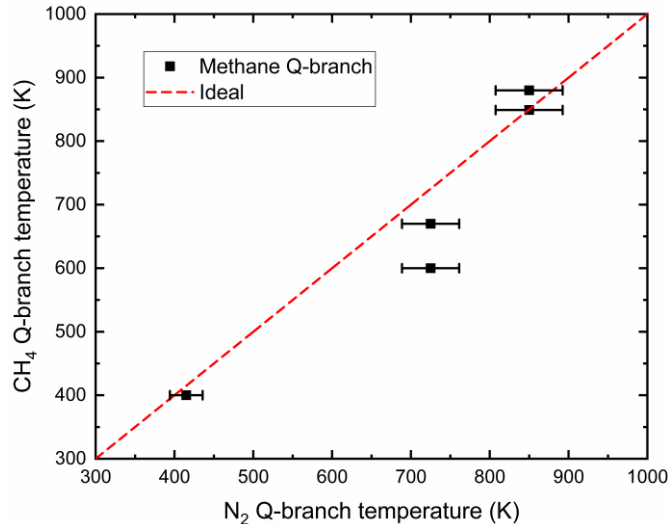


Figure 9. Comparison between the evaluated temperatures from the CH<sub>4</sub> Q-branch and N<sub>2</sub> Q-branch in 500 Torr, 10% CH<sub>4</sub> and 90% N<sub>2</sub> mixtures. Uncertainties in the N<sub>2</sub> Q-branch temperatures are shown as horizontal error bars.

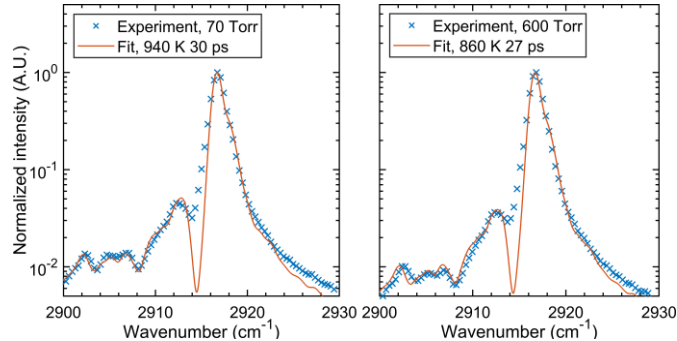


Figure 10. Example fitted CH<sub>4</sub> Q-branch spectra in pure CH<sub>4</sub> at 70 Torr and 600 Torr using a 1000 K furnace setpoint. The intensity axis used log scaling to emphasize the hot band structure.

The good agreement between the CH<sub>4</sub> Q-branch and N<sub>2</sub> Q-branch measurements indicated that the heated cell was not ideal. The evaluated temperatures and the set point temperatures were different by 10 to 25%. Unfortunately, using the same cylindrical focusing optics as in [51] meant that the probe volume was not exactly in the center of the tube furnace and was outside the uniform temperature region specified by the manufacturer. Therefore, heat loss toward the exposed windows of the cell could have caused a discrepancy between the set point temperature and the measured temperature. However, this was only a significant problem at the highest pressures, 500 and 600 Torr, measured in this study. In Fig. 10, example spectra and fits of the 70 Torr and 600 Torr pure CH<sub>4</sub> mixtures at 1000 K are plotted. To emphasize the hot band structure, the temperature axis used log scaling. The dip in the intensity around 2914 cm<sup>-1</sup> is likely due to using a Gaussian line shape for the spectrometer instrument function rather than a Voigt profile. However, since the N<sub>2</sub> Q-branch was fit satisfactorily with a Gaussian line shape, the same instrument function was applied to the CH<sub>4</sub> Q-branch spectrum for consistency. The 70 Torr fitted temperature was 940 K, while the 600 Torr fitted temperature was 860 K. Therefore, at 70 Torr, the difference in measured and setpoint temperature was 6%, while at 600 Torr it was 14%, more than a factor of two larger. This indicates that the time-domain fitting using the set point temperatures as the input parameter at 70 Torr was valid, but some caution should be taken when evaluating the 600 Torr results.

While measurements at atmospheric pressure were not conducted, the pressure linearity of the linewidths indicate that the current fs/ps CH<sub>4</sub> CARS model should be valid up to atmospheric pressure. However, measurements beyond atmospheric pressure will likely require the incorporation of line mixing effects [79] as demonstrated in a high pressure CH<sub>4</sub> ns- CARS study [80]. Use of short probe pulses with pulse widths ranging from 2 to 6 ps like in [57,81] may allow fs/ps CH<sub>4</sub> CARS measurements at pressures of 20 atm or more

### 3.3 Spatially resolved 1-D CH<sub>4</sub> ν<sub>1</sub> Q-branch thermometry

The potential for 1-D measurements as well as to illustrate the radial homogeneity of the heated cell is shown in Fig. 11. In Fig. 11, a spatially resolved 1-D profile of the temperatures were fit for each spatial location. The camera pixels were summed such that each binned pixel corresponded to approximately  $40 \mu\text{m}$  like in [51]. The spatially averaged temperature measurement is plotted as the dashed line and the 1-D temperature profile is within  $\pm 5\%$  of the dashed line. The shaded areas in Fig. 11 are the standard deviations of the temperatures evaluated from each of the 50 measured frames. While this is not a single-shot histogram, it provides a measure of precision of the 1-D measurement. The standard deviation is larger near the edges of the laser sheet due to the limited SNR from the spatial profile of the pump/Stokes beam.

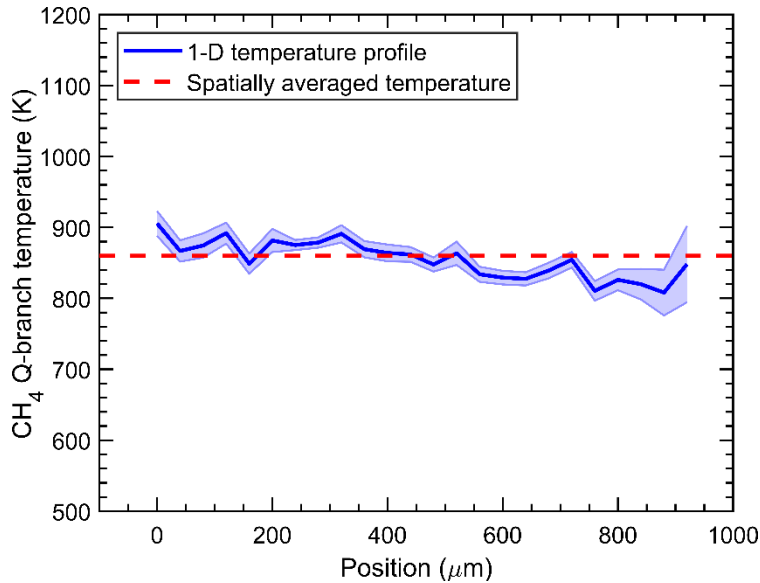


Fig. 11. Spatially resolved 1-D temperature profile within the tube furnace at 600 Torr and 1000 K set point. The shaded error bars are the standard deviations of temperatures evaluated from 50 single images taken with 2 second exposures. The dashed line is the mean spatially integrated temperature evaluated from Fig. 10.

The spatial resolution of the fs/ps CARS measurement in this work was approximately  $0.04 \text{ mm} \times 0.04 \text{ mm} \times 0.5 \text{ mm}$  with a crossing angle of 5 degrees. In the 600 Torr, 1000 K setpoint measurement, a single frame had  $10^5$  counts on the ground state peak and 4000 counts on the largest hot band peak. Converted to a single shot signal-to-noise ratio (SNR) by dividing by 40 laser shots results in a single shot SNR of 2500 and 100, respectively. Detection with an intensified CCD (ICCD) or electron multiplying CCD (EMCCD) would increase the SNR by up to 1000. The SNR is highly dependent on the mole fraction of  $\text{CH}_4$  in the probe region as well as the pressure, temperature, and beam interaction length. We estimate  $\text{CH}_4$  thermometry should be possible with an ICCD or EMCCD at  $\text{CH}_4$  mole fractions of 1% at atmospheric pressure. However, this is dependent on the temperature and correspondingly the  $\text{CH}_4$  hot band intensity. Additional improvements to the setup such as higher bandwidth femtosecond pulses or higher probe pulse energies could push this detection limit even further. To achieve spatial resolution like that of the spontaneous Raman scattering experiments in [27], doubling of the beam crossing angle would be required. This would reduce the signal by at least a factor of 4 and

raise the detection limit by a factor of 2. This trade-off between spatial resolution and signal level is inherent to the CARS diagnostic. The SNR can be improved by increasing the interaction path length, limited only by the coherence length in the case of collinear beams [31].

#### 4. Conclusions and outlook

In this work, we have developed and validated a time dependent CH<sub>4</sub> fs/ps CARS model with experimental probe delay scans for pressures ranging from 70 to 600 Torr and temperatures ranging from 295 K to 1000 K. To our knowledge, this is the first time-domain fs/ps CARS model for a hydrocarbon molecule as well as the first model for a molecule larger than CO<sub>2</sub> [82,83]. The experimental and modelled time delay traces matched well for delays up to 500 ps at 295 K and 200 ps at higher temperatures. At later delays, the coherence beating was qualitatively matched. Exploration of different linewidth models such as energy corrected sudden scaling law (ECS) and use of a more detailed MEG model could improve the fits at later time delays. In addition, fitting the ground state and hot band linewidths separately could be explored to improve the temperature retrieval accuracy. The effect of collisional partner was demonstrated to be negligible for early probe delays before the characteristic molecular collision time. The effect of collisional partner was demonstrated to be negligible for early probe delays. Differences in pure CH<sub>4</sub> and CH<sub>4</sub> mixtures with N<sub>2</sub> and Ar were found to appear only after 100 ps, and a “collision sensitivity time” was defined based on the measured time scale. This time scale was found to be longer than the “collision-free” time but shorter than the mean time between collisions. All time delay scans measured in this study were fit with a decaying exponential function and the total Q-branch linewidths was extracted and tabulated to facilitate future linewidth modelling efforts. Furthermore, we have demonstrated the ability to perform thermometry in the frequency-domain with the CH<sub>4</sub>  $\nu_1$  Q-branch using fs/ps CARS and found that the fitted temperatures corresponded well with those simultaneously measured from the N<sub>2</sub> Q-branch. However, only three high temperature set points were used. Additional measurements at different temperatures, particularly at flame temperatures exceeding 1000 K, would help improve and quantify the accuracy of the CH<sub>4</sub> fs/ps CARS thermometry.

1-D fs/ps CARS thermometry using the CH<sub>4</sub> Q-branch was also demonstrated. The developed model and experimental apparatus described in this work can be readily applied to situations that require localized spatially resolved 1-D measurements of CH<sub>4</sub>. Applications such as catalytic reforming of CH<sub>4</sub> could leverage the ability of fs/ps CARS to measure within 50  $\mu\text{m}$  of a solid surface [50]. Furthermore, common molecules used for thermometry such as N<sub>2</sub> or O<sub>2</sub> may not be in the gas mixture. For instance, chemical looping oxidation of CH<sub>4</sub> does not have any N<sub>2</sub> or O<sub>2</sub> present in the gas phase for synthesis of syngas and carbon sequestration [84]. In addition, at high temperatures, the relatively large Raman cross-section of CH<sub>4</sub> could help overcome sensitivity limits from reductions in density. As a result, probing CH<sub>4</sub> for quantification of concentration and temperature would be both necessary and advantageous. Finally, with this model, non-equilibrium vibrational distribution functions of CH<sub>4</sub> like in [23] may be able to be detected and quantified with 1-D fs/ps CARS imaging. The role of vibrational excitation in plasma catalysis is not well-understood [6,85], and future near-surface measurements would be important for further developments in this area.

## Acknowledgements

We contribute this paper to celebrate Professor Ronald K. Hanson's legacy in laser diagnostics and chemical kinetics. This material is based upon work supported by the U.S. Department of Energy (DOE), Office of Science, Office of Workforce Development for Teachers and Scientists, Office of Science Graduate Student Research (SCGSR) program. The SCGSR program is administered by the Oak Ridge Institute for Science and Education (ORISE) for the DOE under contract number DE-SC0014664. CJK and BMG were supported by the Office of Chemical Sciences, Geosciences, and Biosciences, Office of Basic Energy Sciences, U.S. Department of Energy. Sandia National Laboratories is a multi-mission laboratory managed and operated by National Technology and Engineering Solutions of Sandia, LLC, a wholly owned subsidiary of Honeywell International, Inc., for the U.S. Department of Energy's National Nuclear Security Administration under Contract DE-NA0003525. This paper describes objective technical results and analysis. Any subjective views or opinions that might be expressed in the paper do not necessarily represent the views of the US DOE or the US Government. YJ would like to thank the funding support of DOE Plasma Science Center, NETL UCFER, and National Science Foundation grants. TYC was partially supported by the Program in Plasma Science and Technology Fellowship (PPST). TYC, EK, and YJ acknowledge the support of ExxonMobil through its membership in the Princeton E-affiliates Partnership of the Andlinger Center for Energy and the Environment. The simulations presented in this article were performed on computational resources managed and supported by the Princeton Institute for Computational Science and Engineering and the Office of Information Technology at Princeton University. We thank Brian D. Patterson for his technical assistance in setting up the furnace and cell for the heated CH<sub>4</sub> measurements. We also thank Dr. Thomas Butterworth for providing the CH<sub>4</sub> Raman transition line list used in this work.

## References

- [1] U.S. Energy Information Administration, Annual Energy Outlook 2020, 2020.
- [2] M.I. Khan, T. Yasmin, A. Shakoor, Technical overview of compressed natural gas (CNG) as a transportation fuel, *Renewable and Sustainable Energy Reviews*. 51 (2015) 785–797.
- [3] X. Tu, J.C. Whitehead, Plasma dry reforming of methane in an atmospheric pressure AC gliding arc discharge: Co-generation of syngas and carbon nanomaterials, *International Journal of Hydrogen Energy*. 39 (2014) 9658–9669.
- [4] M. Rezaei, S.M. Alavi, S. Sahebdehfar, P. Bai, X. Liu, Z.-F. Yan, CO<sub>2</sub> reforming of CH<sub>4</sub> over nanocrystalline zirconia-supported nickel catalysts, *Applied Catalysis B: Environmental*. 77 (2008) 346–354.
- [5] L. Wang, Y. Yi, C. Wu, H. Guo, X. Tu, One-Step Reforming of CO<sub>2</sub> and CH<sub>4</sub> into High-Value Liquid Chemicals and Fuels at Room Temperature by Plasma-Driven Catalysis, *Angewandte Chemie International Edition*. 56 (2017) 13679–13683.
- [6] T. Nozaki, K. Okazaki, Non-thermal plasma catalysis of methane: Principles, energy efficiency, and applications, *Catalysis Today*. 211 (2013) 29–38.

- [7] W.-C. Chung, M.-B. Chang, Review of catalysis and plasma performance on dry reforming of CH<sub>4</sub> and possible synergistic effects, *Renewable and Sustainable Energy Reviews*. 62 (2016) 13–31.
- [8] H. de Coninck, A. Revi, M. Babiker, P. Bertoldi, M. Buckeridge, A. Cartwright, W. Dong, J. Ford, S. Fuss, J.-C. Hourcade, Strengthening and implementing the global response, (2018).
- [9] P. Bergamaschi, M. Schupp, G.W. Harris, High-precision direct measurements of <sup>13</sup>CH<sub>4</sub>/<sup>12</sup>CH<sub>4</sub> and <sup>12</sup>CH<sub>3</sub>D/<sup>12</sup>CH<sub>4</sub> ratios in atmospheric methane sources by means of a long-path tunable diode laser absorption spectrometer, *Appl. Opt.*, AO. 33 (1994) 7704–7716.
- [10] V. Nagali, S.I. Chou, D.S. Baer, R.K. Hanson, J. Segall, Tunable diode-laser absorption measurements of methane at elevated temperatures, *Appl. Opt.* 35 (1996) 4026.
- [11] S.-I. Chou, D.S. Baer, R.K. Hanson, Diode laser absorption measurements of CH<sub>3</sub>Cl and CH<sub>4</sub> near 1.65 μm, *Appl. Opt.*, AO. 36 (1997) 3288–3293.
- [12] A.A. Kosterev, R.F. Curl, F.K. Tittel, C. Gmachl, F. Capasso, D.L. Sivco, J.N. Baillargeon, A.L. Hutchinson, A.Y. Cho, Methane concentration and isotopic composition measurements with a mid-infrared quantum-cascade laser, *Opt. Lett.* 24 (1999) 1762.
- [13] S.H. Pyun, J. Cho, D.F. Davidson, R.K. Hanson, Interference-free mid-IR laser absorption detection of methane, *Meas. Sci. Technol.* 22 (2011) 025303.
- [14] R. Sur, S. Wang, K. Sun, D.F. Davidson, J.B. Jeffries, R.K. Hanson, High-sensitivity interference-free diagnostic for measurement of methane in shock tubes, *J. Quant. Spectrosc. Radiat. Transf.* 156 (2015) 80–87.
- [15] N.G. Blume, V. Ebert, A. Dreizler, S. Wagner, Broadband fitting approach for the application of supercontinuum broadband laser absorption spectroscopy to combustion environments, *Meas. Sci. Technol.* 27 (2016) 015501.
- [16] J.J. Barrett, R.F. Begley, Low-power cw generation of coherent anti-Stokes Raman radiation in CH<sub>4</sub> gas, *Appl. Phys. Lett.* 27 (1975) 129–131.
- [17] D.N. Kozlov, A.M. Prokhorov, V.V. Smirnov, The methane ν<sub>1</sub> (a<sub>1</sub>) vibrational state rotational structure obtained from high-resolution CARS-spectra of the Q-branch, *Journal of Molecular Spectroscopy*. 77 (1979) 21–28.
- [18] H. Frunder, D. Illig, H. Finsterhölzl, H.W. Schrötter, B. Lavorel, G. Roussel, J.C. Hilico, J.P. Champion, G. Pierre, G. Poussigue, E. Pascaud, Revised analysis of the structure of the ν<sub>1</sub> band of methane, *Chemical Physics Letters*. 100 (1983) 110–114.
- [19] M. Ridder, A.A. Suvernev, T. Dreier, Collision effects in nitrogen and methane coherent anti-Stokes Raman isotropic Q-branch spectra at high densities, *The Journal of Chemical Physics*. 105 (1996) 3376–3386.
- [20] D. Pieroni, J.-M. Hartmann, F. Chaussard, X. Michaut, T. Gabard, R. Saint-Loup, H. Berger, J.-P. Champion, Experimental and theoretical study of line mixing in methane spectra. III. The Q branch of the Raman ν<sub>1</sub> band, *The Journal of Chemical Physics*. 112 (2000) 1335–1343.
- [21] E. Jourdanneau, T. Gabard, F. Chaussard, R. Saint-Loup, H. Berger, E. Bertseva, F. Grisch, CARS methane spectra: Experiments and simulations for temperature diagnostic purposes, *Journal of Molecular Spectroscopy*. 246 (2007) 167–179.

- [22] E. Jourdanneau, F. Chaussard, R. Saint-Loup, T. Gabard, H. Berger, The methane Raman spectrum from 1200 to 5500 $\text{cm}^{-1}$ : A first step toward temperature diagnostic using methane as a probe molecule in combustion systems, *Journal of Molecular Spectroscopy*. 233 (2005) 219–230.
- [23] T.D. Butterworth, B. Amyay, D. v. d. Bekerom, A. v. d. Steeg, T. Minea, N. Gatti, Q. Ong, C. Richard, C. van Kruijsdijk, J.T. Smits, A.P. van Bavel, V. Boudon, G.J. van Rooij, Quantifying methane vibrational and rotational temperature with Raman scattering, *J. Quant. Spectrosc. Radiat. Transf.* 236 (2019) 106562.
- [24] G. Magnotti, U. Kc, P.L. Varghese, R.S. Barlow, Raman spectra of methane, ethylene, ethane, dimethyl ether, formaldehyde and propane for combustion applications, *J. Quant. Spectrosc. Radiat. Transf.* 163 (2015) 80–101.
- [25] I.E. Gordon, L.S. Rothman, C. Hill, R.V. Kochanov, Y. Tan, P.F. Bernath, M. Birk, V. Boudon, A. Campargue, K.V. Chance, B.J. Drouin, J.M. Flaud, R.R. Gamache, J.T. Hodges, D. Jacquemart, V.I. Perevalov, A. Perrin, K.P. Shine, M.A.H. Smith, J. Tennyson, G.C. Toon, H. Tran, V.G. Tyuterev, A. Barbe, A.G. Császár, V.M. Devi, T. Furtenbacher, J.J. Harrison, J.M. Hartmann, A. Jolly, T.J. Johnson, T. Karman, I. Kleiner, A.A. Kyuberis, J. Loos, O.M. Lyulin, S.T. Massie, S.N. Mikhailenko, N. Moazzen-Ahmadi, H.S.P. Müller, O.V. Naumenko, A.V. Nikitin, O.L. Polyansky, M. Rey, M. Rotger, S.W. Sharpe, K. Sung, E. Starikova, S.A. Tashkun, J.V. Auwera, G. Wagner, J. Wilzewski, P. Wcisło, S. Yu, E.J. Zak, The HITRAN2016 molecular spectroscopic database, *J. Quant. Spectrosc. Radiat. Transf.* 203 (2017) 3–69.
- [26] A. Farooq, J.B. Jeffries, R.K. Hanson, In situ combustion measurements of H<sub>2</sub>O and temperature near 2.5  $\mu\text{m}$  using tunable diode laser absorption, *Measurement Science and Technology*. 19 (2008).
- [27] R.S. Barlow, S. Meares, G. Magnotti, H. Cutcher, A.R. Masri, Local extinction and near-field structure in piloted turbulent CH<sub>4</sub>/air jet flames with inhomogeneous inlets, *Combustion and Flame*. 162 (2015) 3516–3540.
- [28] A. Lo, A. Cessou, P. Vervisch, Space and time analysis of the nanosecond scale discharges in atmospheric pressure air: II. Energy transfers during the post-discharge, *Journal of Physics D: Applied Physics*. 47 (2014) 115202.
- [29] M. Snee, W. Ubachs, Direct measurement of the Rayleigh scattering cross section in various gases, *J. Quant. Spectrosc. Radiat. Transf.* 92 (2005) 293–310.
- [30] W.R. Fenner, H.A. Hyatt, J.M. Kellam, S.P.S. Porto, Raman cross section of some simple gases, *J. Opt. Soc. Am., JOSA*. 63 (1973) 73–77.
- [31] W.M. Tolles, J.W. Nibler, J.R. McDonald, A.B. Harvey, A Review of the Theory and Application of Coherent Anti-Stokes Raman Spectroscopy (CARS), *Appl. Spectrosc., AS*. 31 (1977) 253–271.
- [32] J. Jonuscheit, A. Thumann, M. Schenk, T. Seeger, A. Leipertz, One-dimensional vibrational coherent anti-Stokes Raman-scattering thermometry, *Opt. Lett.* 21 (1996) 1532.
- [33] J.H. Stufflebeam, A.C. Eckbreth, CARS TEMPERATURE AND SPECIES MEASUREMENTS IN PROPELLANT FLAMES, *IJEMCP*. 3 (1994).
- [34] A.C. ECKBRETH, R.J. HALL, CARS Concentration Sensitivity With and Without Nonresonant Background Suppression, *Combustion Science and Technology*. 25 (1981) 175–192.

- [35] F. Vestin, M. Afzelius, P.-E. Bengtsson, Development of rotational CARS for combustion diagnostics using a polarization approach, *Proc. Combust. Inst.* 31 (2007) 833–840.
- [36] G. Marowsky, G. Lüpke, CARS-Background suppression by phase-controlled nonlinear interferometry, *Appl. Phys. B.* 51 (1990) 49–51.
- [37] B.D. Prince, A. Chakraborty, B.M. Prince, H.U. Stauffer, Development of simultaneous frequency- and time-resolved coherent anti-Stokes Raman scattering for ultrafast detection of molecular Raman spectra, *The Journal of Chemical Physics.* 125 (2006) 044502.
- [38] D. Pestov, R.K. Murawski, G.O. Ariunbold, X. Wang, M. Zhi, A.V. Sokolov, V.A. Sautenkov, Y.V. Rostovtsev, A. Dogariu, Y. Huang, M.O. Scully, Optimizing the Laser-Pulse Configuration for Coherent Raman Spectroscopy, *Science.* 316 (2007) 265–268.
- [39] H.U. Stauffer, J.D. Miller, M.N. Slipchenko, T.R. Meyer, B.D. Prince, S. Roy, J.R. Gord, Time- and frequency-dependent model of time-resolved coherent anti-Stokes Raman scattering (CARS) with a picosecond-duration probe pulse, *The Journal of Chemical Physics.* 140 (2014) 024316.
- [40] W.D. Kulatilaka, P.S. Hsu, H.U. Stauffer, J.R. Gord, S. Roy, Direct measurement of rotationally resolved H<sub>2</sub> Q-branch Raman coherence lifetimes using time-resolved picosecond coherent anti-Stokes Raman scattering, *Appl. Phys. Lett.* 97 (2010) 081112.
- [41] A. Bohlin, B.D. Patterson, C.J. Kliewer, Communication: Simplified two-beam rotational CARS signal generation demonstrated in 1D, *The Journal of Chemical Physics.* 138 (2013) 081102.
- [42] A. Bohlin, C.J. Kliewer, Communication: Two-dimensional gas-phase coherent anti-Stokes Raman spectroscopy (2D-CARS): Simultaneous planar imaging and multiplex spectroscopy in a single laser shot, *The Journal of Chemical Physics.* 138 (2013) 221101.
- [43] A. Bohlin, C.J. Kliewer, Two-beam ultrabroadband coherent anti-Stokes Raman spectroscopy for high resolution gas-phase multiplex imaging, *Appl. Phys. Lett.* 104 (2014) 031107.
- [44] S.P. Kearney, D.J. Scoglietti, Hybrid femtosecond/picosecond rotational coherent anti-Stokes Raman scattering at flame temperatures using a second-harmonic bandwidth-compressed probe, *Opt. Lett.* 38 (2013) 833.
- [45] J.D. Miller, S. Roy, J.R. Gord, T.R. Meyer, Communication: Time-domain measurement of high-pressure N<sub>2</sub> and O<sub>2</sub> self-broadened linewidths using hybrid femtosecond/picosecond coherent anti-Stokes Raman scattering, *J. Chem. Phys.* 135 (2011) 201104.
- [46] C.E. Dedic, T.R. Meyer, J.B. Michael, Single-shot ultrafast coherent anti-Stokes Raman scattering of vibrational/rotational nonequilibrium, *Optica.* 4 (2017) 563.
- [47] S.R. Engel, J.D. Miller, C.E. Dedic, T. Seeger, A. Leipertz, T.R. Meyer, Hybrid femtosecond/picosecond coherent anti-Stokes Raman scattering for high-speed CH<sub>4</sub>/N<sub>2</sub> measurements in binary gas mixtures: Hybrid fs/ps CARS for high-speed CH<sub>4</sub>/N<sub>2</sub> measurements, *J. Raman Spectrosc.* 44 (2013) 1336–1343.

- [48] M. Scherman, M. Nafa, T. Schmid, A. Godard, A. Bresson, B. Attal-Tretout, P. Joubert, Rovibrational hybrid fs/ps CARS using a volume Bragg grating for N<sub>2</sub> thermometry, *Opt. Lett.* 41 (2016) 488.
- [49] J.E. Retter, G.S. Elliott, S.P. Kearney, Dielectric-barrier-discharge plasma-assisted hydrogen diffusion flame. Part 1: Temperature, oxygen, and fuel measurements by one-dimensional fs/ps rotational CARS imaging, *Combustion and Flame*. 191 (2018) 527–540.
- [50] A. Bohlin, C. Jainski, B.D. Patterson, A. Dreizler, C.J. Kliewer, Multiparameter spatio-thermochemical probing of flame–wall interactions advanced with coherent Raman imaging, *Proceedings of the Combustion Institute*. 36 (2017) 4557–4564.
- [51] T.Y. Chen, B.M. Goldberg, B.D. Patterson, E. Kolemen, E. Kolemen, Y. Ju, C.J. Kliewer, 1-D imaging of rotation-vibration non-equilibrium from pure rotational ultrafast coherent anti-Stokes Raman scattering, *Opt. Lett., OL*. 45 (2020) 4252–4255.
- [52] J. Kiefer, T. Seeger, S. Steuer, S. Schorsch, M.C. Weikl, A. Leipertz, Design and characterization of a Raman-scattering-based sensor system for temporally resolved gas analysis and its application in a gas turbine power plant, *Meas. Sci. Technol.* 19 (2008) 085408.
- [53] D. Bermejo, J. Santos, P. Cancio, High-resolution q-cw SRS spectrum of 12CH<sub>4</sub> in the region of the level crossing between  $\nu_1$  and  $\nu_2 + \nu_4$ , *Journal of Molecular Spectroscopy*. 156 (1992) 15–21.
- [54] A. Bohm, N.L. Harshman, H. Walther, Relating the Lorentzian and exponential: Fermi’s approximation, the Fourier transform, and causality, *Phys. Rev. A*. 66 (2002) 012107.
- [55] S.P. Kearney, P.M. Danehy, Pressure measurements using hybrid femtosecond/picosecond rotational coherent anti-Stokes Raman scattering, *Opt. Lett., OL*. 40 (2015) 4082–4085.
- [56] D. Escofet-Martin, A.O. Ojo, J. Collins, N.T. Mecker, M. Linne, B. Peterson, Dual-probe 1D hybrid fs/ps rotational CARS for simultaneous single-shot temperature, pressure, and O<sub>2</sub>/N<sub>2</sub> measurements, *Opt. Lett., OL*. 45 (2020) 4758–4761.
- [57] J.D. Miller, S. Roy, J.R. Gord, T.R. Meyer, Communication: Time-domain measurement of high-pressure N<sub>2</sub> and O<sub>2</sub> self-broadened linewidths using hybrid femtosecond/picosecond coherent anti-Stokes Raman scattering, *J. Chem. Phys.* 135 (2011) 201104.
- [58] C.J. Kliewer, A. Bohlin, E. Nordström, B.D. Patterson, P.-E. Bengtsson, T.B. Settersten, Time-domain measurements of S-branch N<sub>2</sub>–N<sub>2</sub> Raman linewidths using picosecond pure rotational coherent anti-Stokes Raman spectroscopy, *Appl. Phys. B*. 108 (2012) 419–426.
- [59] A. Hosseinnia, M. Ruchkina, P. Ding, P.-E. Bengtsson, J. Bood, Simultaneous temporally and spectrally resolved Raman coherences with single-shot fs/ns rotational CARS, *Opt. Lett., OL*. 45 (2020) 308–311.
- [60] S. Roy, P.S. Hsu, N. Jiang, J.R. Gord, W.D. Kulatilaka, H.U. Stauffer, J.R. Gord, Direct measurements of collisionally broadened Raman linewidths of CO<sub>2</sub> S-branch transitions, *J. Chem. Phys.* 138 (2013) 024201.
- [61] H. Graener, J.W. Nibler, A. Laubereau, Picosecond coherent anti-Stokes Raman spectroscopy of molecules in free jet expansions, *Opt. Lett.* 9 (1984) 165.

- [62] H. Graener, A. Laubereau, High resolution Fourier transform Raman spectroscopy with ultrashort laser pulses, *Optics Communications*. 54 (1985) 141–146.
- [63] M.L. STREKALOV, Rotational energy relaxation in CH<sub>4</sub> and CH<sub>4</sub>-He, Ar collisions calculated from coherent and stimulated Raman spectroscopy data, *Molecular Physics*. 100 (2002) 1049–1056.
- [64] L. Martinsson, P. Bengtsson, M. Aldén, S. Kröll, J. Bonamy, A test of different rotational Raman linewidth models: Accuracy of rotational coherent anti-Stokes Raman scattering thermometry in nitrogen from 295 to 1850 K, *The Journal of Chemical Physics*. 99 (1993) 2466–2477.
- [65] T. Seeger, F. Beyrau, A. Bräuer, A. Leipertz, High-pressure pure rotational CARS: comparison of temperature measurements with O<sub>2</sub>, N<sub>2</sub> and synthetic air: High-pressure pure rotational CARS, *J. Raman Spectrosc.* 34 (2003) 932–939.
- [66] J.R. Hetzler, J.I. Steinfeld, State-to-state rotational energy transfer measurements in silane by infrared double resonance with a tunable diode laser, *J. Chem. Phys.* 92 (1990) 7135–7155.
- [67] J.J. Klaassen, S.L. Coy, J.I. Steinfeld, Ch. Roche, State-to-state rotational energy transfer measurements in methane (CH<sub>4</sub>) by infrared double resonance with a tunable diode laser, *J. Chem. Phys.* 100 (1994) 5519–5532.
- [68] B. Foy, J. Hetzler, G. Millot, J.I. Steinfeld, State-to-state rotational energy transfer in methane (13CD<sub>4</sub>) from infrared double-resonance experiments with a tunable diode laser, *J. Chem. Phys.* 88 (1988) 6838–6852.
- [69] Ch. Wenger, J.P. Champion, Spherical top data system (STDS) software for the simulation of spherical top spectra, *J. Quant. Spectrosc. Radiat. Transf.* 59 (1998) 471–480.
- [70] L.A. Rahn, R.E. Palmer, Studies of nitrogen self-broadening at high temperature with inverse Raman spectroscopy, *J. Opt. Soc. Am. B*. 3 (1986) 1164.
- [71] M.L. Koszykowski, L.A. Rahn, R.E. Palmer, M.E. Coltrin, Theoretical and experimental studies of high-resolution inverse Raman spectra of molecular nitrogen at 1–10 atm, *J. Phys. Chem.* 91 (1987) 41–46.
- [72] G. Tarrago, M. Dang-Nhu, G. Poussigues, G. Guelachvili, C. Amiot, The ground state of methane 12CH<sub>4</sub> through the forbidden lines of the ν<sub>3</sub> band, *Journal of Molecular Spectroscopy*. 57 (1975) 246–263.
- [73] A. Chakraborty, D.G. Truhlar, J.M. Bowman, S. Carter, Calculation of converged rovibrational energies and partition function for methane using vibrational–rotational configuration interaction, *J. Chem. Phys.* 121 (2004) 2071–2084.
- [74] J.J. Klaassen, S.L. Coy, J.I. Steinfeld, B. Abel, Direct measurement of rotational and vibrational relaxation in methane overtone levels by time-resolved infrared double-resonance spectroscopy, *The Journal of Chemical Physics*. 101 (1994) 10533–10547.
- [75] F. Menard-Bourcin, L. Doyennette, J. Menard, C. Boursier, Time-Resolved IR–IR Double Resonance Measurements in Methane Excited to 2ν<sub>3</sub> (F<sub>2</sub>), *J. Phys. Chem. A*. 104 (2000) 5444–5450.
- [76] T.L. Courtney, C.J. Kliewer, Rotational coherence beating in molecular oxygen: Coupling between electronic spin and nuclear angular momenta, *J. Chem. Phys.* 149 (2018) 234201.
- [77] C.-J. Chen, M.H. Back, R.A. Back, The Thermal Decomposition of Methane. I. Kinetics of the Primary Decomposition to C<sub>2</sub>H<sub>6</sub> + H<sub>2</sub>; Rate Constant for the

- Homogeneous Unimolecular Dissociation of Methane and its Pressure Dependence, *Can. J. Chem.* 53 (1975) 3580–3590.
- [78] A. Esposito, M. Lappa, G. Zuppari, C. Allouis, B. Apicella, M. Commodo, P. Minutolo, C. Russo, On the Formation and Accumulation of Solid Carbon Particles in High-Enthalpy Flows Mimicking Re-Entry in the Titan Atmosphere, *Fluids*. 5 (2020) 93.
- [79] R.J. Hall, J.F. Verdieck, A.C. Eckbreth, Pressure-induced narrowing of the cars spectrum of N<sub>2</sub>, *Optics Communications*. 35 (1980) 69–75.
- [80] F. Grisch, E. Bertseva, M. Habiballah, E. Jourdanneau, F. Chaussard, R. Saint-Loup, T. Gabard, H. Berger, CARS spectroscopy of CH<sub>4</sub> for implication of temperature measurements in supercritical LOX/CH<sub>4</sub> combustion, *Aerospace Science and Technology*. 11 (2007) 48–54.
- [81] T.L. Courtney, N.T. Mecker, B.D. Patterson, M. Linne, C.J. Kliewer, Hybrid femtosecond/picosecond pure rotational anti-Stokes Raman spectroscopy of nitrogen at high pressures (1–70 atm) and temperatures (300–1000 K), *Appl. Phys. Lett.* 114 (2019) 101107.
- [82] M. Kerstan, I. Makos, S. Nolte, A. Tünnermann, R. Ackermann, Two-beam femtosecond coherent anti-Stokes Raman scattering for thermometry on CO<sub>2</sub>, *Appl. Phys. Lett.* 110 (2017) 021116.
- [83] M. Gu, A. Satija, R.P. Lucht, CO<sub>2</sub> chirped-probe-pulse femtosecond CARS thermometry, *Proc. Combust. Inst.* (2020).
- [84] T. Mattisson, A. Järtnäs, A. Lyngfelt, Reactivity of Some Metal Oxides Supported on Alumina with Alternating Methane and Oxygen Application for Chemical-Looping Combustion, *Energy Fuels*. 17 (2003) 643–651.
- [85] P. Mehta, P. Barboun, F.A. Herrera, J. Kim, P. Rumbach, D.B. Go, J.C. Hicks, W.F. Schneider, Overcoming ammonia synthesis scaling relations with plasma-enabled catalysis, *Nat Catal.* 1 (2018) 269–275.